

# Horizontal-axis tidal turbine design based on 3D hydrodynamics

Zohreh Sarichloo, Pedram Ghorbanpour, and Francesco Salvatore

**Abstract**—A computational procedure for the hydrodynamic analysis and design of horizontal-axis tidal turbines is presented and numerical applications are discussed. The methodology combines an original design algorithm and a turbine hydrodynamics model valid for arbitrary 3D flows. Different from standard design methods based on blade element models, 3D-flow corrections are not necessary. Blade geometry parameters are determined with the objective to maximize power at given design Tip Speed Ratio (TSR), whereas a constraint is introduced in order to limit turbine thrust at TSR higher than the design condition. Numerical applications include the design of a laboratory-scale turbine and a full-scale turbine for the exploitation of tidal streams in the Messina strait. Alternative design solutions obtained by varying the design TSR are compared in terms of energy output as well as mechanical loads transferred to the powertrain.

**Index Terms**—Marine renewable energy, tidal turbines, design, hydrodynamics, boundary integral equation model, annual energy production.

## NOMENCLATURE

Symbol (Latin)	Description
$c, C$	blade chord
$D, C_D$	drag, drag coefficient
$D, R$	turbine diameter, radius
$D_H$	hub diameter
$F_t$	tangential force
$F_x$	axial force
$L, C_L$	lift, lift coefficient
$n$	rotational speed (round/sec)
$p, C_p$	pressure, pressure coefficient
$P, C_P$	power, power coefficient
$Q, C_Q$	torque, torque coefficient
$T, C_T$	thrust, thrust coefficient
$V, V_0$	inflow velocity
$Z$	number of blades

Symbol (Greek)	Description
$\alpha$	angle of attack
$\alpha_{des}$	design angle of attack
$\alpha_e$	effective angle of attack
$\beta$	pitch angle
$\lambda$	tip speed ratio
$\lambda_{des}$	design tip speed ratio
$\lambda_r$	$\lambda \cdot r/R$
$\phi$	inflow angle
$\rho$	density
$\sigma$	rotor solidity
Abbreviation	Description
AEP	Annual Energy production
AoA	Angle of Attack
BEM	Blade Element Method
BIEM	Boundary Integral Equation Model
LLM	Lifting Line Method
MPPT	Maximum Power Point Tracking
MT	Momentum Theory
RANS	Reynolds Averaged Navier Stokes
TSR	Tip Speed Ratio
VFC	Viscous Flow Correction

## I. INTRODUCTION

THE design of a hydrokinetic turbine is a multi-disciplinary problem in which the accurate definition of rotor hydrodynamic performance is of primary importance since the early stages of device development.

Fast and robust models suitable for recursive calculations are widely used at the cost of reduced capability to describe the relevant physics. A classical design approach derived from aeronautical propellers and wind turbines is based on hydrodynamic models combining momentum theory and Blade Element Methods (BEM), see *e.g.*, [1] and [2]. The optimal distribution of inflow angle at blade sections is determined under simplifying assumptions and, by guessing a suitable distribution of the angle of attack, the blade pitch distribution to maximize turbine power follows. The angle of attack corresponding to the maximum lift to drag ratio of blade sections under two-dimensional (2D) flow assumptions is typically considered as the optimal condition. Once the pitch angle is determined, the chord distribution is obtained accordingly [3]. The effect of other geometry parameters like blade number, solidity, section thickness and camber, can be studied through parametric design, as discussed *e.g.*, in [4], or through multi-objective optimization [5].

The main limitation of this type of design methodologies is that BEM hydrodynamics is based on simplified flow assumptions. In particular, semi-empirical

Manuscript received December 30th, 2021, published 10 June 2022.

This is an open access article distributed under the terms of the Creative Commons Attribution 4.0 licence (CC BY <http://creativecommons.org/licenses/by/4.0/>). Unrestricted use (including commercial), distribution and reproduction is permitted provided that credit is given to the original author(s) of the work, including a URI or hyperlink to the work, this public license and a copyright notice. This article has been subject to single-blind peer review by a minimum of two reviewers.

This work was partially supported by the ULYSSES project funded by CNR (DIT.AD019.040).

Zohreh Sarichloo (zohreh.sarichloo@insean.cnr.it), Pedram Ghorbanpour (pedram.ghorbanpour@inn.cnr.it) and Francesco Salvatore (francesco.salvatore@cnr.it) are with the Institute of Marine Engineering (former INSEAN) of the Italian National Research Council (CNR), Via di Vallerano, 139, I-00128 Rome, Italy.

Digital Object Identifier: <https://doi.org/10.36688/imej.5.77-90>

corrections are considered to account for three-dimensional flow effects at blade root and tip and blade-to-blade interactions [6].

Hydrodynamics models for three-dimensional (3D) inviscid flows, represent a more physically consistent approach than BEM, whereas computational effort is comparably small, as necessary for recursive calculations in design studies. Lifting Line Method (LLM) and Boundary Integral Equation Method (BIEM) fall within this class and applications to hydrokinetic turbines have been addressed, *e.g.*, in [7] and [8]. Although these models are widely used for marine propellers, a few applications to marine turbine design are reported. In [9] and [10] LLM and BIEM are applied to design marine turbine blades with optimal distribution of circulation along the span.

The inclusion of full 3D hydrodynamics by BIEM in horizontal-axis turbine design problems is the subject of the present work. The methodology developed in [8] adopts a general inviscid-flow formulation to describe unsteady hydrodynamics under arbitrary inflow conditions. By including trailing vorticity and Viscous-Flow Correction (VFC) models, accurate predictions of turbine performance can be obtained over a wide range of operating conditions, as discussed in [11]. In the present application to design, BIEM-VFC is combined with an original approach to determine blade shape parameters matching given design objectives and constraints. Using optimal conditions from 2D-flow hydrodynamics and momentum theory only as initial guess, radial distributions of blade pitch and chord are iteratively modified in order to maximize the power coefficient at design tip speed ratio, with a condition to limit the thrust coefficient over a given operational range.

Two applications of the proposed methodology are presented. First, the development of a model turbine for experimental research at laboratory scale is addressed. Next, the results of the preliminary design of a full-scale turbine are presented and the impact of design solutions in terms of energy output as well as mechanical loads transferred to the powertrain are discussed.

The manuscript is structured as follows. The design methodology is derived in Section II, whereas Section II describes the BIEM-VFC hydrodynamic model. The numerical application to the design of a model-scale turbine is discussed in Section IV. The impact of design parameters on the operation and annual energy production of a full-scale turbine in a tidal site is analyzed in Section V. Concluding remarks and future work to improve the present methodology are discussed in Section VI.

## II. DESIGN METHODOLOGY

A design methodology for horizontal-axis hydrokinetic turbines is developed. This consists of a computational procedure to determine the shape of turbine blades that maximize performance parameters under imposed constraints and given operating conditions.

For a turbine with diameter  $D$ , inflow speed  $V$ , rotor rotational speed  $\Omega = 2\pi n$ , main operational and performance parameters are:

$$\begin{aligned} \lambda &= \frac{\Omega R}{V}, && \text{Tip Speed Ratio (TSR)} \\ C_T &= \frac{T}{\frac{1}{2}\rho AV^2}, && \text{Thrust coefficient} \\ C_Q &= \frac{Q}{\frac{1}{2}\rho AV^2 R}, && \text{Torque coefficient} \\ C_P &= \frac{2\pi n Q}{\frac{1}{2}\rho AV^3} = \lambda \cdot C_Q, && \text{Power coefficient} \end{aligned} \quad (1)$$

where  $T, Q$  are, respectively, rotor thrust and torque,  $\rho$  is the water density, and  $A = \pi R^2$  is the rotor swept area with  $R = D/2$  the rotor radius.

The design problem is formulated here through the definition of:

- **design conditions:** inflow speed  $V$ , rotor rotational speed  $n$  (rps),
- **design parameters:** blade pitch, chord, maximum thickness and camber radial distributions,
- **design objectives:** maximize power coefficient at given design operating point,
- **design constraints:** limit thrust coefficient over a given  $\lambda$  range.

Recalling the present study deals with the hydrodynamic design of turbine blades, design parameters include only geometry quantities. Rotor diameter, nacelle diameter  $D_H$ , number of blades  $Z$ , and blade section baseline profile are geometry parameters that are prescribed and kept fixed during the design procedure. From design conditions the design tip speed ratio  $\lambda_{des} = \Omega R/V$  is defined.

The proposed procedure integrates three modules by an iterative scheme, as sketched in Fig. 1.

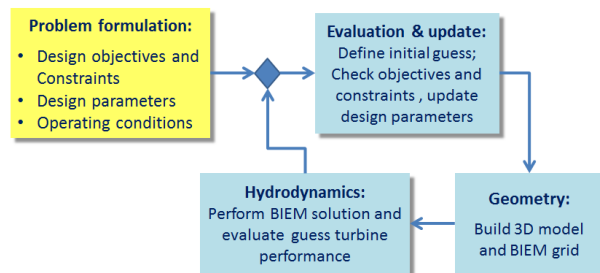


Fig. 1. Problem formulation and main modules of the computational design procedure.

The core of the methodology is the **Evaluation and Update module** in which starting from an initial guess, design parameters are modified to match design objectives and constraints. Next, the **Geometry module** elaborates design parameters to create a 3D model of the guess turbine and build the computational grid that is passed as input to the **Hydrodynamics module** where BIEM-VFC simulations of the turbine flow are performed. Performance parameters evaluated by BIEM-VFC are sent as input to the Evaluation and Update module for a new iteration. In the following, details of the Evaluation and Update module are given.

Geometry and Hydrodynamics modules are briefly described in Section III.

#### A. Definition of the design angle of attack

Following a common approach in wind/marine turbine design, a main assumption in the procedure is that turbine performance objectives are achieved when blade sections operate at an *optimal* Angle of Attack (AoA), hereafter denoted as the design AoA,  $\alpha_{des}$ . The radial distribution of the quantity  $\alpha_{des}$  is unknown and an original approach is used here to derive it from the analysis of sectional lift and drag contributions to blade torque and thrust.

Inflow and sectional contributions to blade loads for two representative blade sections are sketched in Fig. 2. In particular, the left picture describes a section close to the blade root, whereas the right picture describes a section close to the blade tip. Moving along blade span from root to tip, both the inflow angle  $\phi$  and the angle  $\gamma$  between the sectional hydrodynamic force  $d\mathbf{F}$  and the rotor axis reduce. The quantity  $d\mathbf{F}$  denotes the force generated by a blade segment of infinitesimal span  $dr$ . This elementary force can be decomposed into axial and in-plane (tangential) contributions, respectively  $dF_x$  and  $dF_t$ , or into lift and drag contributions, respectively  $dL$  and  $dD$ .

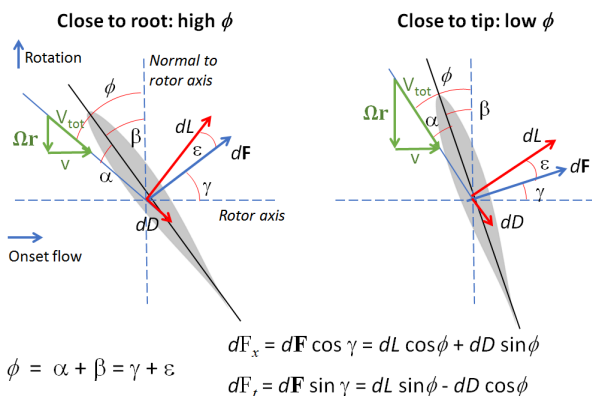


Fig. 2. Inflow and elementary load contributions at representative blade sections at root (left) and tip (right).

Design requirements for maximum power and limited thrust are obtained by maximizing the  $d\mathbf{F}$  component along the tangential direction. This corresponds to different conditions along the blade span. Close to the root, the inflow angle is relatively high and this limits the sectional contribution to thrust,  $dT = dF_x$ . In this portion of the blade, sections can operate at relatively high angle of attack  $\alpha$  and deliver a net contribution to torque,  $dQ = r dF_t$ . Moving to the blade tip, the inflow angle becomes small and the projection of the hydrodynamic force  $d\mathbf{F}$  along the tangential direction is small. In this portion of the blade, sections should operate at AoA corresponding to the highest lift-to-drag ratio  $dL/dD$  in order to minimize the passive torque contribution associated to drag  $dD$ . It should be noted that sketches in left and right Fig. 2 are also representative of conditions at, respectively, low and high  $\lambda$  for a blade section at a given radius.

This characterization of the force contributions along blade span can be used to identify the range of AoA where blade sections should operate in order to maximize performance.

Specifically, two conditions are determined:

- inner sections or low  $\lambda$ : AoA above maximum lift-to-drag ratio and below maximum lift conditions,
- outer sections or high  $\lambda$ : AoA above minimum drag and below maximum lift-to-drag ratio conditions.

A design AoA distribution  $\alpha_{des}(r)$  satisfying these conditions is then applied in the present design procedure. Sectional contributions to lift and drag along blade span are evaluated by 3D-flow BIEM-VFC hydrodynamics. Assuming the unperturbed inflow speed  $V$  is constant, at each step of the iterative procedure turbine flow predictions are performed over a full range of  $\lambda$  values. By sweeping from low to high  $\lambda$  values, each blade section at a given radius undergoes a variation of the AoA from high to low values. The range of variation depends on the  $\lambda$  range considered. As an example, in the numerical application described in Section IV, it is approximately  $1 < \lambda < 11$  and this corresponds to  $-8 < \alpha < 25$ . Combining solutions at different  $\lambda$ , it is possible to determine the relationship between angle of attack and sectional lift, drag, and lift/drag ratio along the blade span. Design AoA conditions as maximum lift, maximum lift/drag ratio, or minimum drag, are summarized in Table I. It is important to notice that using full 3D hydrodynamics by BIEM-VFC, the induced drag due to the trailing vorticity shed by blades is implicitly accounted for. This non-negligible contribution is typically neglected in BEM-based formulations. In addition to  $\alpha_{des}$  definitions based on full 3D hydrodynamics, the AoA corresponding to the maximum lift/drag ratio of blade section profiles under 2D-flow assumptions is also considered. In the present work, the 2D-flow X-Foil code [12] is used to determine this quantity.

TABLE I  
BLADE LOADING CONDITIONS USED TO DEFINE DESIGN AO A DISTRIBUTIONS.

Reference	Description	Source
CLMAX	maximum sectional lift	BIEM-VFC
CDMIN	minimum sectional drag	BIEM-VFC
L2DMAX	maximum sectional lift/drag ratio	BIEM-VFC
L2DMAX-2D	maximum sectional lift/drag ratio	X-Foil (2D)

#### B. Design procedure

Once the problem of interest is formulated through the definition of design conditions, the first step is to determine an initial guess of the blade geometry. A profile geometry is chosen to define baseline thickness and camber chordwise distributions to build the blade sections. A database of the baseline profile lift and drag curves over relevant ranges of AoA and inflow speed (Reynolds number) is generated. In the present study, the numerical evaluation of the baseline profile lift and drag curves is obtained by using the X-Foil code [12].

Initial blade pitch and chord distributions are determined from optimal conditions derived by the momentum theory under simplified assumptions. Introducing  $\lambda_r = 2\pi n r / V = \lambda \cdot r / R$ , the optimal conditions for the inflow angle at radius  $r \in [r_h, R]$  yield

$$\phi_{opt}^{2D}(r) = \frac{2}{3} \arctg(1/\lambda_r), \quad (2)$$

whereas the optimal distribution of chord is

$$c_{opt}^{2D}(r) = 8\pi r \left(1 - \cos(\phi_{opt}^{2D})\right) / \left(ZC_L^{2D}\right) \quad (3)$$

where  $C_L^{2D}$  is the lift coefficient of the blade section at radius  $r$  from the 2D-flow data. Alternative expressions of blade chord distributions can be derived as described, e.g., in [3].

The initial design AoA radial distribution  $\alpha_{des}^{2D}$  follows from conditions in Table I in which 2D-flow lift and drag curves in the baseline profile database are used in place of 3D hydrodynamics data that is still not available. The initial guess radial pitch distribution is then evaluated as

$$\beta(r) = \phi_{opt}^{2D}(r) - \alpha_{des}^{2D}(r) \quad (4)$$

Once pitch and chord are determined, the initial definition of blade geometry parameters is completed by imposing the position of each section leading edge point along the local pitch line. In addition to this, blade section offsets are determined by imposing radial distributions of thickness and camber. Such a blade geometry parametrization is used in the geometry module (Fig. 1) to build a 3D model of the initial guess rotor by combining the blades and a nacelle with given length  $L_h$  and diameter  $D_h$ . A computational grid discretizing nacelle and blades surfaces is built and passed to the hydrodynamics module for BIEM-VFC calculations.

Turbine hydrodynamics predictions are performed over a full  $\lambda$  range from deep stall to free-wheeling conditions. For each  $\lambda$  value, both global performance as well as local flow quantities are evaluated:

- global quantities: thrust, torque, power coefficients, respectively,  $C_T, C_Q, C_P$ ,
- local quantities: radial distributions of sectional lift and drag, effective angle of attack  $\alpha_e$ .

The term *effective* is used to stress that the angle of attack  $\alpha_e$  is evaluated by considering the rotor wake-induced velocity field predicted by the BIEM-VFC solution. Combining results for all  $\lambda$  cases, relationships among blade loading and effective AoA are built and the initial definition of the design AoA radial distribution based only on 2D-flow data is updated with 3D-flow effects included. All the quantities evaluated by BIEM-VFC at a discrete number of  $\lambda$  values are interpolated to determine radial distributions at the  $\lambda_{des}$  of interest, and a new iteration begins.

At iterations  $i > 0$ , the inflow angle  $\phi$  is updated by considering the pitch angle and the effective AoA evaluated by BIEM-VFC at the previous iteration

$$\phi^{(i)}(r) = \beta^{(i-1)}(r) + \alpha_e^{(i-1)}(r) \quad (i > 0) \quad (5)$$

A new guess of the pitch distribution is obtained by evaluating the deviation between the design AoA,  $\alpha_{des}$  and the effective AoA,  $\alpha_e$ . At convergence of the procedure, the difference between effective and design AoA should reduce to zero throughout the blade span. Denoting this difference by  $\Delta\alpha$ , Eq. (4) is recast as

$$\begin{aligned} \Delta\alpha^{(i)}(r) &= \alpha_e^{(i-1)}(r) - \alpha_{des}^{(i)}(r) \quad (i > 0) \\ \beta^{(i)}(r) &= \beta^{(i-1)}(r) + \Delta\alpha^{(i)}(r) \end{aligned} \quad (6)$$

where at iteration  $i = 1$ ,  $\beta^{(i-1)}$  follows from Eq. (4).

The chord distribution is updated by using an expression equivalent to Eq. (3) where the inflow angle and the sectional lift are obtained from the BIEM-VFC solution including 3D-flow effects

$$c^{(i)}(r) = 8\pi r \left(1 - \cos(\phi^{(i-1)})\right) / \left(ZC_L^{(i-1)}\right) \quad (7)$$

The new pitch and chord distributions are used to update the 3D model of the guess blade and the procedure is iterated. If no constraints are applied, the iteration continues until the difference  $\Delta\alpha$  between effective and design AoA distributions goes to zero along the blade span. It should be noted that conditions (5) to (7) are enforced at the imposed  $\lambda_{des}$ .

### C. Performance maximization and thrust constraint

In order to deliver the design results matching practical requirements, the present procedure embeds the possibility to account for constraints on turbine loading over a range of operating conditions. The case of interest here is to limit the thrust that is generated by the turbine. A design constraint is imposed that at convergence of the iterative procedure, the slope of the thrust coefficient curve at  $\lambda$  higher than the peak power point shall satisfy the condition

$$\left| \frac{\partial C_T}{\partial \lambda} \right| \leq \delta_{CT} \quad (\lambda > \lambda_0) \quad (8)$$

where  $\delta_{CT}$  is a given small value. In the numerical procedure, this condition is imposed by evaluating an average of the  $C_T$  curve slope in the  $\lambda$  region  $\lambda_0 < \lambda < \lambda_{max}$ , where  $\lambda_{max}$  is the highest  $\lambda$  value considered in the BIEM-VFC analysis, and  $\lambda_0 = 1/2(\lambda_{des} + \lambda_{max})$ .

The achievement of condition (8) is obtained through a decision-making algorithm that at each iteration determines an update of the design AoA distribution. Specifically, at the  $i$ -th iteration, two cases are possible:

- case 1:  $\partial C_T / \partial \lambda$  is negative
- case 2:  $\partial C_T / \partial \lambda$  is positive

(A zero derivate condition is numerically reduced to one of the two cases above). Case 1) means that the current design AoA distribution  $\alpha_{des}^{(i)}$  determines through Eq.(6) a pitch distribution that results into blade unloading at  $\lambda > \lambda_0$ . Then, the  $\alpha_{des}^{(i)}$  distribution is modified by increasing the angle of attack in the attempt to increase further blade loading inasmuch the constraint on thrust is not violated. The new guess of the design AoA is then assigned as

$$\alpha_{des}^{(i+1)} = \alpha_{des}^{(i)} + \Delta\xi \quad (9)$$

where  $\Delta\xi$  is a positive value proportional to the distance of the current  $C_T$  slope value from the imposed threshold  $\delta_{CT}$ .

Similarly, when case 2) occurs, the current design AoA distribution determines a pitch distribution corresponding to blade overloading. The new design condition is determined from eq. (9) where quantity  $\Delta\xi$  is negative and proportional to the distance of the  $C_T$  slope value from the imposed threshold  $\delta_{CT}$ . Condition (8) is taken as the convergence criterium of the whole design procedure.

To summarize, at each step of the iterative procedure the following radial distributions are updated:

- pitch,  $\beta(r)$ , by Eqs. (4) ( $i = 0$ ) and (6) ( $i > 0$ )
- chord,  $c(r)$ , by Eqs. (3) ( $i = 0$ ) and (7) ( $i > 0$ ),
- design AoA,  $\alpha_{des}(r)$ , through Eq (9).

A flow-chart visualizing the algorithm implemented into the design procedure is given in Fig. (3). It is worth to observe that the decision-making algorithm to satisfy condition (8) can be adapted to manage other conditions as, *e.g.*, the negative pressure peak at blade leading edge, that is taken as an indicator of the cavitation risk.

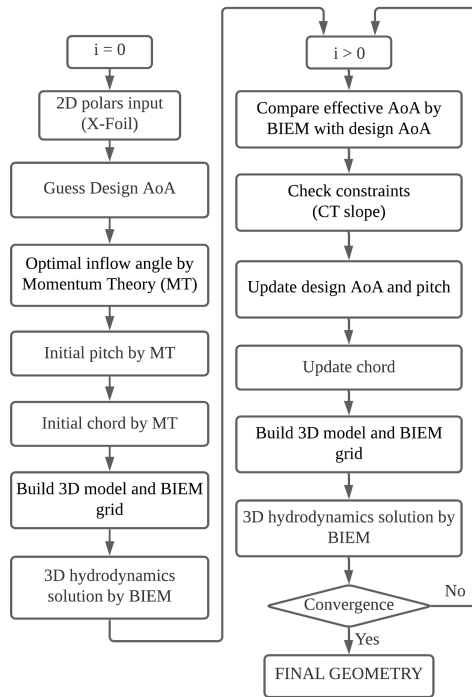


Fig. 3. Design procedure: main steps at start ( $i = 0$ ) and during iteration ( $i > 0$ ).

### III. 3D TURBINE MODEL AND HYDRODYNAMICS BY BIEM-VFC

The utilization of BIEM-VFC hydrodynamics implies that at each step of the iterative procedure a complete 3D model of the turbine is generated and a computational grid is built. In the present approach, only radial distributions of blade pitch and chord are varied during the iterative procedure. All the other geometry quantities are initially prescribed and kept fixed, with

exception of blade section offsets that depend on the guessed chord length.

Nacelle and blade surfaces are discretized into quadrilateral elements to build the computational grid necessary for the numerical solution of BIEM-VFC equations. Figure 4 shows an example of the 3D model of a three-bladed turbine with cylindrical nacelle, and the corresponding surface grid. Both 3D model and surface grid are built by a fully-automated procedure that is repeated at each iteration.

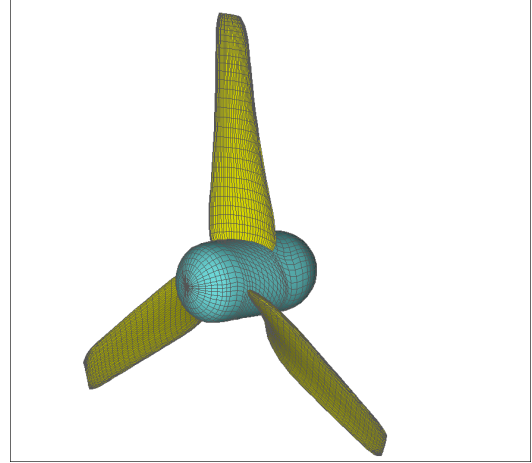


Fig. 4. Example of computational grid for turbine hydrodynamics predictions by BIEM-VFC

3D-flow hydrodynamics by BIEM-VFC is a distinguishing feature of the present design methodology. Details of this computational model can be found in previous work by the authors, see *e.g.* [8], whereas key aspects are briefly reviewed here. BIEM is valid under inviscid flow assumptions to describe the flowfield around a lifting body in an arbitrary onset flow. The induced velocity field is represented as the gradient of a scalar potential  $\varphi$  that follows from the solution of the Laplace equation by a boundary integral formulation. A trailing-wake model allows to describe the vorticity generation and shedding mechanism that is associated with the formation of inviscid loads on blades. Under attached flow conditions, pressure  $p$  evaluated by the Bernoulli theorem provides an accurate description of normal stress over the blade surface, as discussed in [11] by comparing BIEM predictions with results by RANS. An example of this comparative study is given in Fig. (5) for two representative cases.

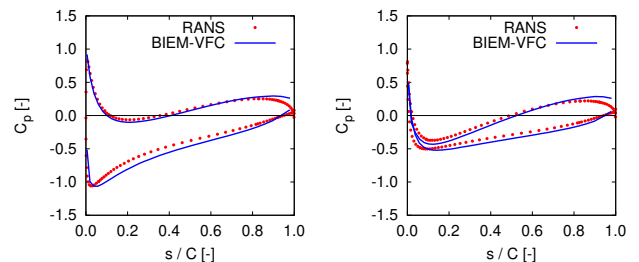


Fig. 5. BIEM prediction of pressure coefficient  $C_p = (p - p_0) / \frac{1}{2} \rho V^2$  as function of non-dimensional chordwise abscissa  $s/C$  compared with RANS [11]. 3-bladed turbine,  $r/R = 0.7$ ,  $\lambda=5$  (design point, left) and  $\lambda = 8$  (overspeed, right).

A partial correction of blade sectional loads is obtained by coupling BIEM with a suitable Viscous Flow Correction Model (VFC). Inviscid-flow lift and drag forces generated at blade sections are modified to include the effects of friction and flow separation and stall under 2D flow conditions at equivalent angle of attack and Reynolds number. Validation studies in [13] demonstrate that by including the VFC model, BIEM allows to determine reliable predictions of blade loads over a wide range of variation of the Reynolds number.

Of particular importance in the present application to design, previous work by the authors analyzed the capability of BIEM-VFC to capture the effects of blade pitch variations on performance. Results in Fig. (6) reproduced from [14] show a fair agreement between BIEM-VFC and experimental data in [15] for a range of variation of blade pitch setting between 20 and 30 degrees, with 20 deg the design condition.

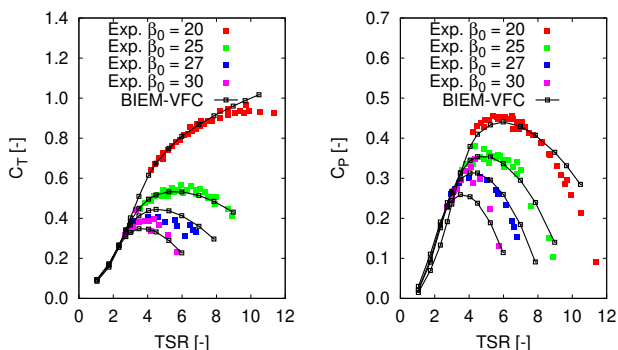


Fig. 6. Thrust (left) and power (right) coefficient curves of a model turbine with variable pitch over a 10 deg range. BIEM-VFC results from [14] compared with experimental data in [15].

The accuracy of BIEM-VFC predictions is significantly affected by the geometry of the trailing wake. Accurate flowfield predictions are obtained by determining the path of trailing vortices as part of the solution through an iterative wake-alignment procedure, as discussed in [11]. A faster approximated description of wake geometry can be obtained by prescribing the wake geometry by semi-empirical models.

In the present study, the prescribed-wake approach has been preferred in order to reduce the computational effort required by the iterative design process. Uniform inflow conditions are considered, and fast steady-state solutions are obtained in a reference frame fixed with rotating blades. The evaluation of turbine performance over a full  $\lambda$  range is completed in less than 1 minute on a standard desktop computer. This represents more than 95% of the computational time required for a single iteration.

#### IV. APPLICATION OF THE DESIGN PROCEDURE: LABORATORY-SCALE MODEL ROTOR

The proposed methodology is applied here to a representative design problem. The objective is to analyze the effect of main geometry parameters on turbine performance and how the configuration that better satisfies the imposed objectives and constraints can be identified.

The proposed design problem deals with the definition of a  $D = 0.7$  m model turbine for experimental research at laboratory scale. The model turbine is intended for activity in the hydrodynamics testing infrastructures at CNR-INM, where large-scale model turbines can be tested in a flow-speed range between 1.0 and 3.0 m/s [17]. The main design requirement is to deliver peak power in a prescribed  $\lambda$  region whereas thrust is kept limited over a full range of operating conditions. The condition on thrust is motivated to avoid excessive axial loads beyond the capacity of thrust sensors during tests at high inflow speed. Under these conditions, blade overloading is also responsible for rotor vibrations and for the occurrence of cavitation at ambient pressure. These phenomenologies are a typical source of uncertainty in measured performance parameters and should be avoided. Design conditions are summarized in Table II.

TABLE II  
MODEL TURBINE DESIGN CONDITIONS.

Rotor diameter, $D$	0.7 m
Nacelle diameter ratio, $D_H/D$	0.20
Number of blades, $Z$	3
Baseline profile	Worthmann FX 63-137
Nominal inflow speed, $V_0$	2.0 m/s
Design TSR, $\lambda_{des}$	between 2.5 and 7.0
Max. thickness distribution, $t_{max}$	imposed, see Fig. 8
Max. camber distribution, $f_{max}$	imposed, see Fig. 8

As baseline profile for the definition of blade sections, normalized thickness and camber chordwise distributions are derived from the Worthmann FX 63-137 geometry [16]. The two distributions denoted respectively by  $t_0$ ,  $f_0$  are plotted in Fig. 7.

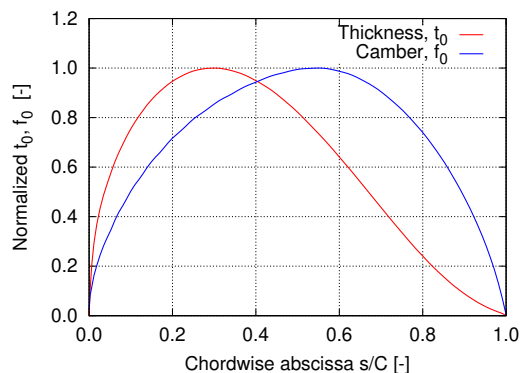


Fig. 7. Model turbine: Worthmann FX normalized thickness and camber chordwise distributions.

Assuming material strength is not a primary concern at model scale, radial distributions of maximum thickness and camber, respectively  $t_{max}$ ,  $f_{max}$ , are preliminarily defined and kept constant in the design process, see Fig. 8. In particular, maximum thickness decreases from 16% at root to 7% at tip, with  $t_{max} = 13.5\%$  at  $r/R = 0.7$ . It should be noted that such thickness distribution is not representative of full scale devices where thick sections at root are necessary for structural integrity. The camber distribution has an average value of 0.06 over most of the blade span and reduces at

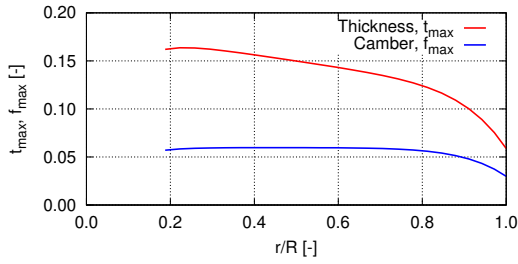


Fig. 8. Model turbine: baseline profile maximum thickness and camber radial distributions (blade root at  $r/R = 0.2$ ).

tip. With this parametrization, blade section offsets  $y$  at radius  $r$  are expressed as

$$y(s, r) = \mp 0.5 t_0(s) \cdot t_{max}(r) + f_0(s) \cdot f_{max}(r) \quad (10)$$

where  $s \in (0, 1)$  is the chordwise abscissa and sign "+" or "-" denote blade suction or pressure side.

In order to evaluate the viscous-flow correction in the BIEM-VFC model as described in Section III, the baseline profile with  $t_{max} = 0.135$  and  $f_{max} = 0.06$  is investigated over a relevant range of both angle of attack and Reynolds number  $Re = VC/\nu$ , where  $V$  is the inflow speed,  $C$  is the profile chord and  $\nu$  the kinematic viscosity of water. Profile lift and drag coefficients,  $C_L$ ,  $C_D$  and efficiency  $C_L/C_D$  are predicted by the X-Foil code [12]. A high-AoA extrapolation model is applied as described in [8].

Results in Fig. 9 show that the reference profile is characterized by high maximum lift and high  $L/D$  ratio in a narrow range of angle of attack. The effect of Reynolds number is apparent for  $Re < 1 \cdot 10^6$ . In particular, a significant variation of the  $L/D$  ratio with the Reynolds number is observed. This phenomenology is typical of profiles with relatively high camber. For turbine operating conditions of interest here,  $V_0 = 2$  m/s and  $D = 0.7$  m/s, preliminary calculations have shown that in the range  $2 < \lambda < 10$ , the chord-based Reynolds number  $Re = c\sqrt{V^2 + (2\pi nr)^2}/\nu$  spans approximately between  $2 \cdot 10^5$  and  $9 \cdot 10^5$ . In the same  $\lambda$  range, the effective AoA spans between  $-5$  and  $20$  degrees.

Recalling the procedure described in Section II-C to update the design AoA, a definition of the range of variation of  $\alpha_{des}$  is required as input.

The following conditions are considered (Table I)

- blade root:  $\alpha_{des}$  between conditions CLMAX and L2DMAX;
- blade tip:  $\alpha_{des}$  between conditions L2DMAX and CDMIN;

Representative radial distributions of the design AoA,  $\alpha_{des}$  for conditions as to maximum lift, maximum lift/drag ratio, or minimum drag, are shown in Fig. 10. The  $\alpha_{des}$  values at root and tip are interpolated along blade span by Hermite 3rd-order polynomials with zero slope at boundaries. Design AoA distributions derived from baseline profile 2D-flow lift and drag curves in Fig. 9 are used only at iteration 1 of the procedure. In the following steps, the conditions are determined from 3D-flow lift and drag distributions obtained by BIEM-VFC and updated according to Eq. (9).

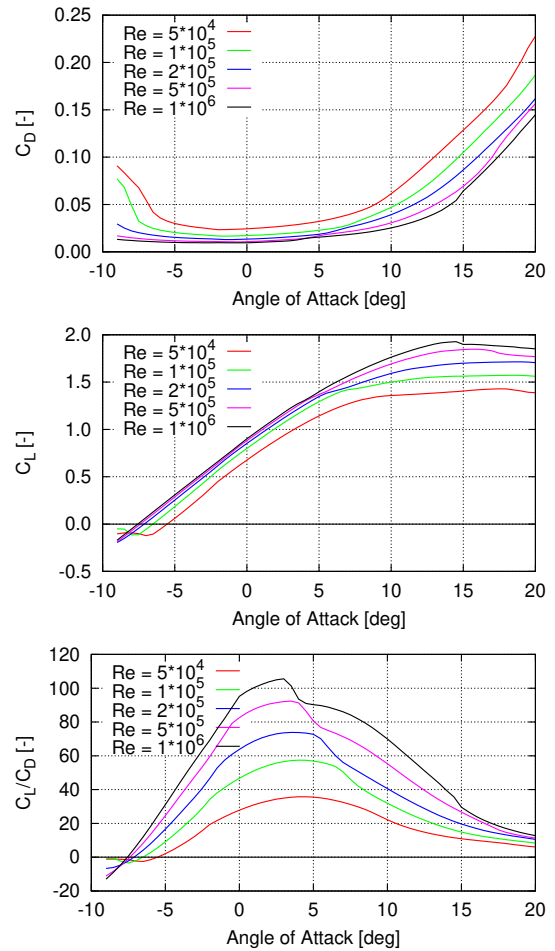


Fig. 9. Baseline profile,  $t_{max} = 0.135$  and  $f_{max} = 0.06$ : drag, lift coefficients  $C_L$ ,  $C_D$ , and efficiency  $C_L/C_D$  as function of AoA and Reynolds number. Numerical predictions by X-Foil code.

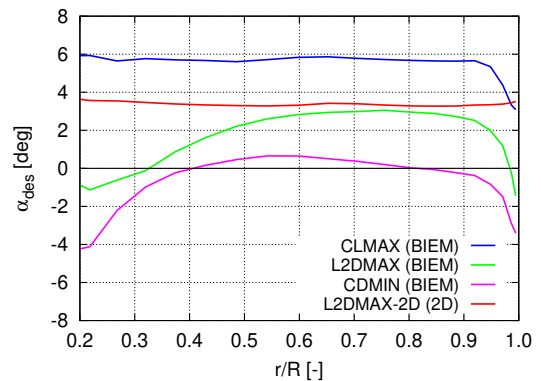


Fig. 10. Example of design AoA radial distributions as from Table I evaluated by BIEM-VFC and by X-Foil during the iterative procedure.

BIEM-VFC calculations are performed for 15  $\lambda$  values in the range between 1.5 and 11.5. Each guess blade is discretized with 18 elements along chord from leading edge to trailing edge and 20 elements along the span, with grid refinement at leading edge, root and tip. The spanwise discretization determines the discrete representation of the radial distribution of all quantities involved in the design procedure. Figure 11 presents a 3D view of one of the designed rotors ( $\lambda_{des} = 4.2$ ). In particular, the trailing wake and the pressure distribu-

tion on blades by BIEM-VFC are shown.

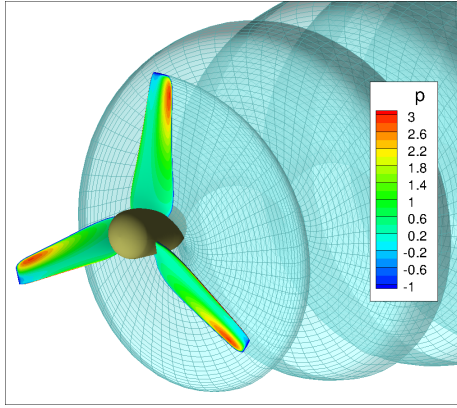


Fig. 11. Model turbine: 3D view of  $\lambda_{des} = 4.2$  rotor with trailing wake and blade pressure distribution evaluated by BIEM-VFC.

The design TSR,  $\lambda_{des}$ , is taken as a parameter that is varied between 2.6 and 7.0, and design loops for each  $\lambda_{des}$  value are performed. With these problem settings, the design procedure delivers a family of rotor geometries corresponding to different  $\lambda_{des}$  values.

The evolution of turbine thrust and power coefficients from the initial guess geometry to convergence of the iterative procedure is illustrated in Figs. 12 and 13 for two representative cases of the  $\lambda_{des}$  parameter:  $\lambda_{des} = 3.0$  and 5.0. For the sake of clarity, a limited number of iteration steps is plotted.

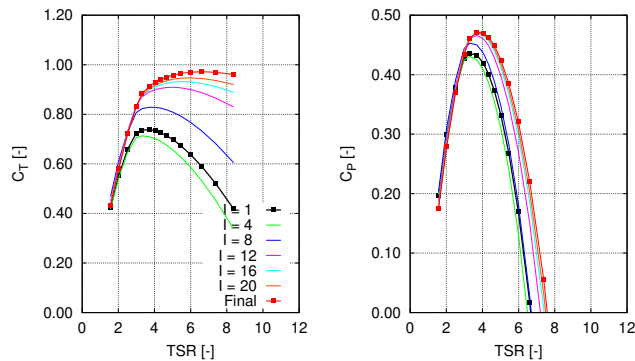


Fig. 12. Model turbine: thrust (left) and power (right) coefficient curves during iteration,  $\lambda_{des} = 3.0$ .

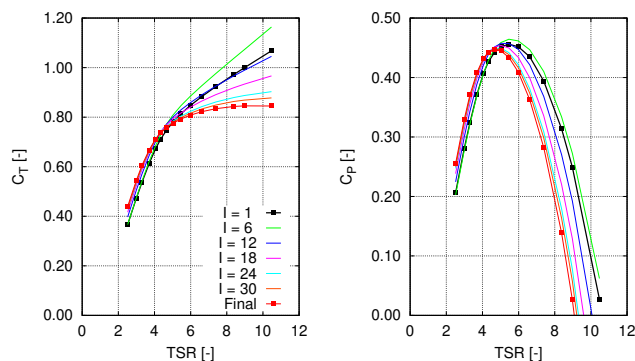


Fig. 13. Model turbine: thrust (left) and power (right) coefficient curves during iteration,  $\lambda_{des} = 5.0$ .

Comparing the two cases reveals a different convergence behaviour. Specifically, in the  $\lambda_{des} = 3.0$

case, the initial guess geometry obtained from optimal conditions based on 2D-flow hydrodynamics and momentum theory, Eqs. (2) to (4), determines a  $C_T$  curve with a negative slope in the operational  $\lambda$  range (case  $I = 1$  in left Fig. 12). This corresponds to blade underloading with respect to the imposed constraint on thrust curve slope. At following iterations, the initial design AoA is varied by Eq. (9) to increase blade loading. This yields an increase of both thrust and power values. At convergence, the highest  $C_P$  value during iteration is achieved.

In the  $\lambda_{des} = 5.0$  case, Fig. 13, the initial guess condition ( $I = 1$ ) yields large blade loading with undesired high thrust coefficients in the high  $\lambda$  range. Then, the design AoA is iteratively varied to reduce blade loading. This yields a marked reduction of  $C_T$  for  $\lambda$  higher than 5-6, whereas  $C_P$  is only marginally penalized.

The comparison between these two cases explains how the imposed constraint on thrust slope affects the results of the design procedure. The general trend found in the present study is that the forced reduction of blade loading is paid by a limitation of power. This effect is significant in cases with a relatively high design  $\lambda$ . The condition on thrust slope could be relaxed in order to allow for a moderate  $C_T$  increase in the high  $\lambda$  region. This is expected to determine a higher  $C_P$  also with high  $\lambda_{des}$  settings. The impact of blade section profile characteristics on turbine thrust and power generation over the  $\lambda$  range is also an important aspect that requires a detailed analysis which is the subject of future work.

A  $\delta_{C_T} \leq 3 \cdot 10^{-3}$  condition is applied in Eq. (8) as convergence criterium. Extensive calculations have shown that when this condition is reached, power coefficient curves as well as radial distributions of geometry parameters present negligible variations as the iteration continues. Close-up of power coefficient curves in the peak region during iteration for the two  $\lambda_{des}$  cases above are given in Fig. 14.

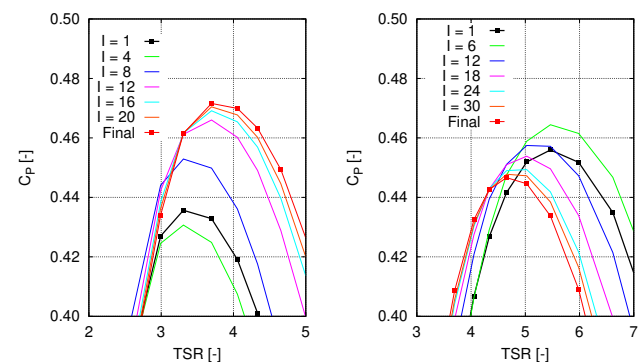


Fig. 14. Model turbine: convergence of power coefficient curves in the peak power region at  $\lambda_{des} = 3.0$  (left) and  $\lambda_{des} = 5.0$  (right).

The condition (8) on thrust curve slope  $\partial C_T / \partial \lambda$  plays a major role in the iterative procedure. The convergence of quantity  $\partial C_T / \partial \lambda$  for all the  $\lambda_{des}$  cases is depicted in Fig. 15. At given steps, the design AoA is updated by Eq. (9) to match the constraint on the thrust curve slope and then kept fixed for a number  $N_{PI}$  of

iterations in order to let the pitch angle converge in Eq. (6). In the present study,  $N_{PI} = 4$  has been used. Figure 15 clearly shows that the largest variations of the  $C_T$  slope occur at steps when the design AoA is updated. Convergence is reached with a variable number of iterations approximately between 25 and 60, with the larger number of iterations typically required for cases at the highest and lowest  $\alpha_{des}$  values. In these extreme cases, calculated  $\alpha_{des}$  radial distributions are sometimes not smooth and this may cause a lack of convergence or unrealistic blade pitch distributions.

Convergence histories of pitch and chord at 70% of blade span are depicted, respectively, in top and bottom Fig. 16. Considering the pitch angle, initial guess values from momentum theory present large differences as  $\lambda_{des}$  increases from 2.6 to 7.0. Such unrealistic trend is significantly mitigated during the iteration and Eq. (6) is used. Considering chord (bottom Fig. 16), the effect of parameter  $\lambda_{des}$  is apparent, as it will be described at the end of the present Section (bottom Fig. 19).

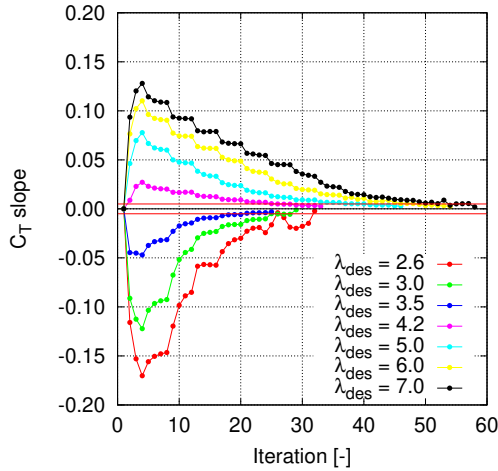


Fig. 15. Model turbine: convergence history of  $C_T$  slope for  $\lambda_{des}$  values from 2.6 to 7.0.

Blade chord evaluated from Eq. (7) presents a quite smooth convergence, as shown in bottom Fig. 16. Results at  $\lambda_{des} = 4.2$  and higher show that during the iteration, the chord length tends to increase from the initial definition, Eq. (3). An opposite trend is found in the lower  $\lambda_{des}$  range. In the present study, the update of chord length by Eq. (7) is performed from iteration  $i = 2N_{PI} = 8$  in order to avoid excessive variations of blade geometry during the first iterations where the largest variations of the pitch angle occur.

Results describing designed rotors performance and geometry parameters for all  $\lambda_{des}$  cases are presented in Figs. 17 to 20. The comparison of performance curves allows to determine the *best* design result. As an example, using the maximum peak power coefficient  $C_{Pmax}$  as the decision criterium, the best performance is found to occur for low  $\lambda_{des}$  values, while a moderate reduction of peak power is observed at higher  $\lambda_{des}$ , see the plot in the middle of Fig. 17. Thrust curves (left) are rather flat at  $\lambda$  higher than the peak power point, as a consequence of the constraint applied to the slope of the thrust coefficient, as described in Section II-C. This

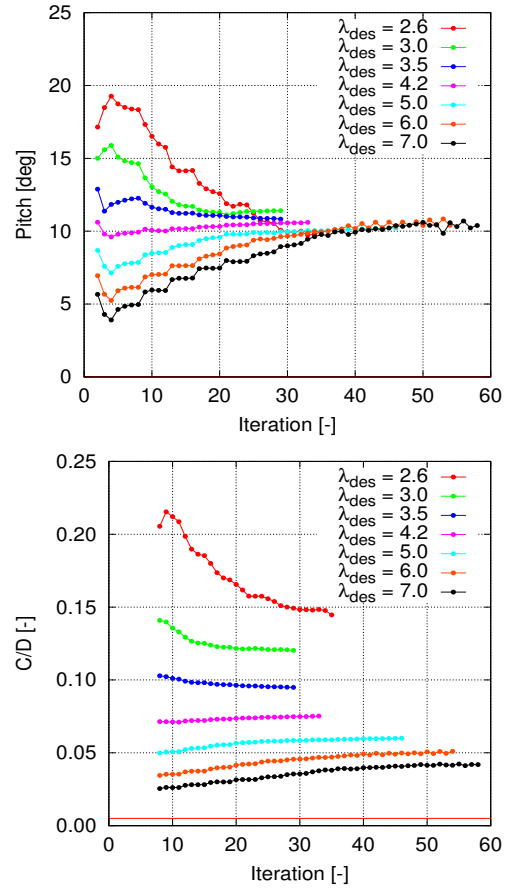


Fig. 16. Model turbine: convergence history of pitch angle  $\beta$  (top) and chord length  $c/D$  (bottom), at  $r/R = 0.7$ ;  $\lambda_{des}$  values from 2.6 to 7.0.

condition limits the loading on turbine blades as the  $\lambda_{des}$  increases, and this motivates the relative reduction of  $C_{Pmax}$  at high  $\lambda_{des}$ . However, the reduction of peak power with  $\lambda_{des}$  is comparatively smaller than the reduction of thrust. This can be seen from the turbine power/thrust ratio  $\eta = C_P/C_T$  plotted in right Fig. 17, with the highest values obtained in the high  $\lambda_{des}$  cases.

Peak values of power coefficient  $C_{Pmax}$ , of power/thrust ratio  $\eta_{max}$  and of the corresponding  $\lambda$  values, respectively,  $\lambda_{CPmax}$  and  $\lambda_{\eta max}$  are given in Table III. By interpolating results from calculated  $\lambda_{des}$  cases, the highest  $C_{Pmax}$  of 0.473 at  $\lambda_{CPmax} = 3.89$  is found.

TABLE III  
MODEL TURBINE: PEAK PERFORMANCE AT DIFFERENT DESIGN  $\lambda_{des}$ .

$\lambda_{des}$	$C_{Pmax}$	$\lambda_{CPmax}$	$\eta_{max}$	$\lambda_{\eta max}$
2.6	0.461	3.5	0.496	3.1
3.0	0.472	3.8	0.521	3.2
3.5	0.470	4.1	0.555	3.3
4.2	0.461	4.4	0.586	3.4
5.0	0.447	4.7	0.614	3.5
6.0	0.425	5.0	0.641	3.7
7.0	0.404	5.3	0.659	3.8

By comparing results at different  $\lambda_{des}$ , it is possible to determine the condition where  $\lambda_{des}$  and  $\lambda_{CPmax}$  are equal. Tip speed ratio values corresponding to peak power and peak power/thrust ratio conditions are plotted versus  $\lambda_{des}$  in Fig. 18. The  $\lambda_{CPmax} = \lambda_{des}$

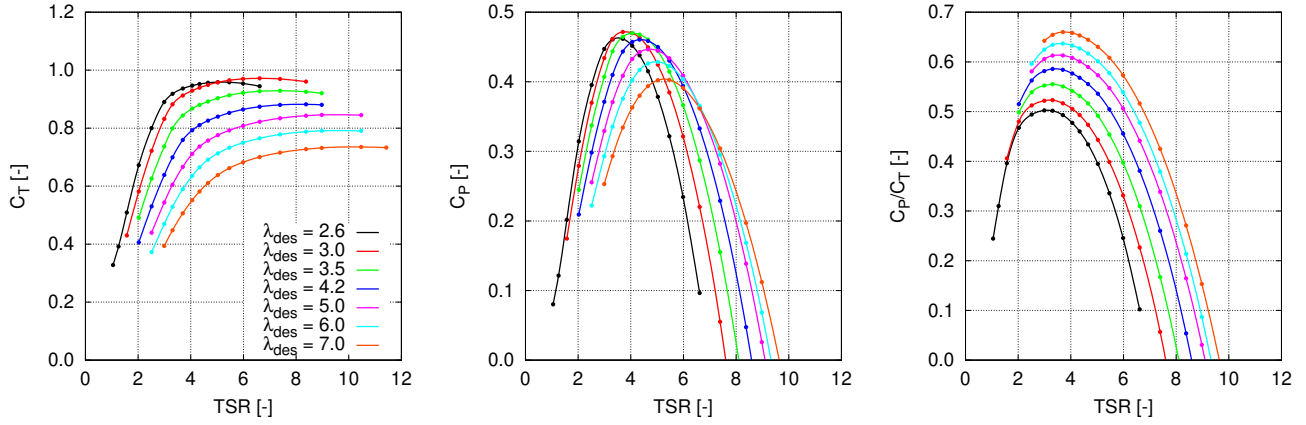


Fig. 17. Model turbine: thrust  $C_T$ , power  $C_P$  coefficients and efficiency  $C_P/C_T$  for  $\lambda_{des}$  values from 2.6 to 7.0.

condition is met for  $\lambda_{des} = 4.6$ , while the condition  $\lambda_{\eta max} = \lambda_{des}$  occurs at  $\lambda_{des} = 3.3$ .

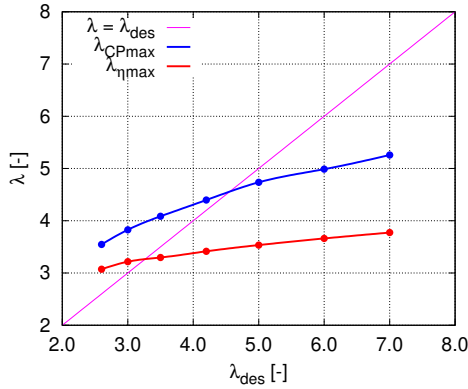


Fig. 18. Model turbine: peak power  $\lambda_{CPmax}$  and peak power/thrust ratio  $\lambda_{\eta max}$  versus  $\lambda_{des}$ .

Figure 19 illustrates pitch  $\beta$  and chord  $c$  radial distributions resulting from the design procedure for all the  $\lambda_{des}$  cases. The blade root section is placed at  $r/R = 0.2$  (Table II). Both pitch and chord distributions are fairly smooth, with the only exception of case  $\lambda_{des} = 2.6$  where a small hump at  $0.65 < r/R < 0.75$  is observed. Comparing pitch distributions, top Fig. 19, larger variations among different  $\lambda_{des}$  cases occur from root to  $r/R = 0.75$ , with larger pitch as  $\lambda_{des}$  decreases, whereas for  $r/R > 0.75$  an opposed trend is observed with small differences of about 1 deg among  $\lambda_{des}$  cases.

Next, bottom Fig. 19 depicts the chord distribution obtained by using Eq. (7). As expected, the blade chord reduces as  $\lambda_{des}$  increases. This aspect can be better studied by introducing the rotor solidity  $\sigma$

$$\sigma = \frac{Z}{\pi R^2} \int_{R_H}^R c(r) dr \quad (11)$$

where  $R_H = D_H/2$  is the blade root radius. Rotor solidity of geometries obtained at different  $\lambda_{des}$ , are presented in left Fig. 20. Next, right Fig. 20 shows the relationship between rotor solidity and maximum power coefficient. The highest value of the power coefficient is delivered by a rotor with solidity  $\sigma = 0.217$ .

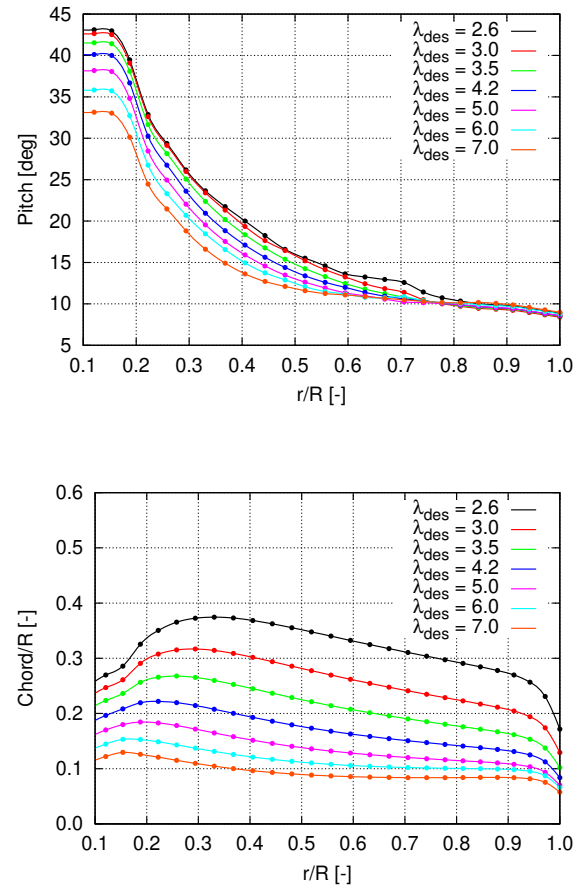


Fig. 19. Model turbine: radial distributions of pitch  $\beta$  (top) and non-dimensional chord  $c/R$  (bottom) for  $\lambda_{des}$  values from 2.6 to 7.0.

The pitch distributions presented above include a smoothing correction in the tip region ( $r/R > 0.95$ ). This is done to overcome local irregularities of flow quantities in the BIEM-VFC solution that may occur in a narrow region at the blade tip during the iterative procedure. In addition to that, a prescribed chord length reduction factor at the blade root and tip is imposed.

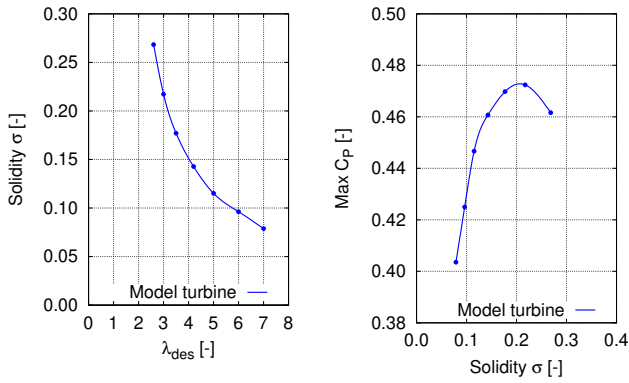


Fig. 20. Model turbine: rotor solidity  $\sigma$  as function of  $\lambda_{des}$  (left), and maximum power coefficient  $C_{Pmax}$  as function of solidity (right).

## V. EFFECT OF DESIGN SOLUTIONS ON FULL-SCALE OPERATION IN A TIDAL SITE

In the model scale turbine study described in the previous section,  $\lambda_{des}$  is taken as a parameter and a series of alternative geometries is obtained. In this section, the comparison among alternative solutions is analyzed further by considering turbine performance factors that are relevant for the operation of full-scale devices in real conditions.

The analysis is carried out by simulating turbine operation in a tidal site with given resource characteristics. The case of interest is the Messina strait between Sicily and mainland Italy in the Mediterranean, Fig. 21. This area, while presenting resource conditions suitable for tidal energy exploitation projects, is characterized by an intense vessel traffic. Environmental conditions are not favorable for the deployment of sea-based mega-watt scale devices [18], whereas submerged floating devices in sheltered areas have been considered [19], [20]. In the present analysis, the installation of a floating barge supporting a cluster of 100 kW-scale turbines in the Ganzirri site (right Fig. 21) is considered. Between 2001 and 2015, this location has hosted the Kobold vertical-axis turbine, the first of its type to have been connected to the grid globally [21].

Tidal resource data for the Ganzirri site are derived from the Tide tables issued yearly by the Hydrology Institute of the Italian Navy [22]. Current velocity measurements are taken in the proximity of the water surface.

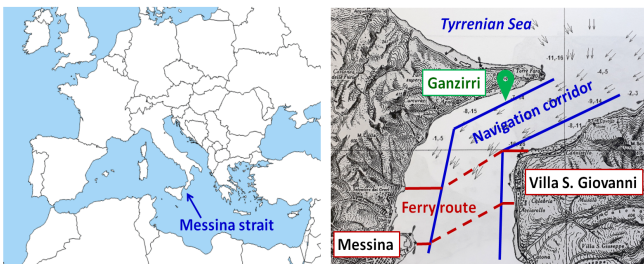


Fig. 21. Messina strait: non-exploitable areas reserved for navigation and Ganzirri site location shown by the green pin.

IN the present analysis, the time series covering a two-month period are considered as approximately representative of the annual resource distribution. Top

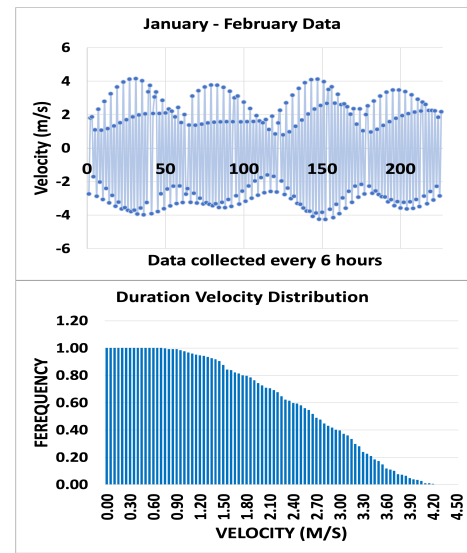


Fig. 22. Current time series at Ganzirri, Messina strait (top), and probability of exceedance (PoE) of current speed (bottom).

Fig. 22 presents peak current speed variability in flood and ebb cycles, whereas the probability of exceedance (PoE) of current speed occurrence between 0 and 4.5 m/s is depicted in bottom Fig. 22. The probability to have an onset flow speed between 2 and 2.5 m/s is between 50 and 70%, which is consistent with turbine operation at nominal flow speed  $V_{des} = 2.5$  m/s.

Performance results of the laboratory-scale design presented in Section IV can be used to obtain a preliminary estimate of the rotor-diameter/rated-power relationship of a true-scale turbine operating at a given nominal flow speed. Considering as example  $C_{Pmax} = 0.47$  (case  $\lambda_{des} = 3.5$  in Table III), a 5 m diameter rotor is expected to deliver 75 kW at a nominal speed of 2.5 m/s. This estimate is approximated as scaling effects in performance curves in Fig. 17 are not considered. Main site characteristics and  $D = 5$  m turbine operational data are summarized in Table IV.

TABLE IV  
TIDAL SITE CONDITIONS.

Tidal site position	Lat. $38^{\circ}15' N$ , Long. $15^{\circ}38' E$
Average water depth, $H$	45 m
Design flow speed, $V_{des}$	2.5 m/s
Rotor diameter, $D$	5.0 m
Rotor immersion, $z_0$	1.5 $D$

Similarly to the model-scale case, the full-scale design is carried out by imposing  $2.6 < \lambda_{des} < 6.8$ . Except for diameter and nominal flow speed, design conditions are equal to those considered in the model-scale design, Table II.

Performance curves of the designed full-scale rotors are given in Fig. 23. Turbine thrust and power coefficients (left and central plots) present a quite similar trend for different values of the  $\lambda_{des}$  parameter as in model-scale design results. Right Fig. 23 shows turbine torque coefficient curves that are further analyzed later. A comparison between design results at full scale and model scale as a function of the  $\lambda_{des}$  parameter is presented in Fig. 24. A 3 to 6% higher peak  $C_p$  values

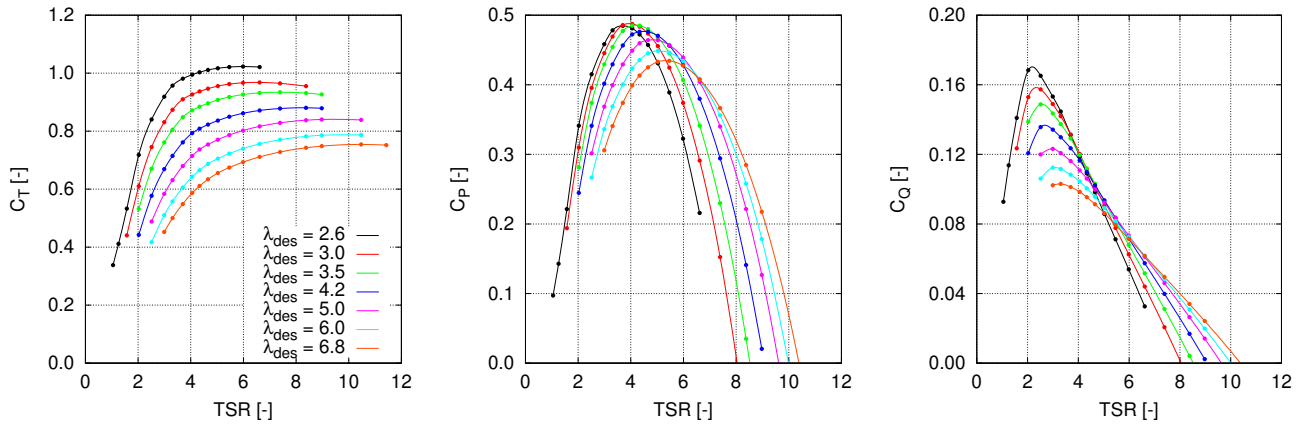


Fig. 23. Full-scale turbine: thrust, power and torque coefficient curves for  $\lambda_{des}$  values from 2.6 to 6.8.

for the full-scale rotors are found in all  $\lambda_{des}$  cases, as shown in left Fig. 24. The peak condition occurs at  $\lambda$  values that are comparable with those observed at model scale, see right Fig. 24. This result is interpreted as the effect of Reynolds number approximately 7 times higher at full scale than model scale. A quantitative comparison of main geometry and performance figures of the design solutions with the highest  $C_{Pmax}$  values is summarized in Table V. Turbine solidity and performance data in the table are derived by interpolating the results obtained at the considered  $\lambda_{des}$  values. Both model and full scale  $C_{Pmax}$  values are apparently high and should be validated by experimental techniques or by CFD modelling.

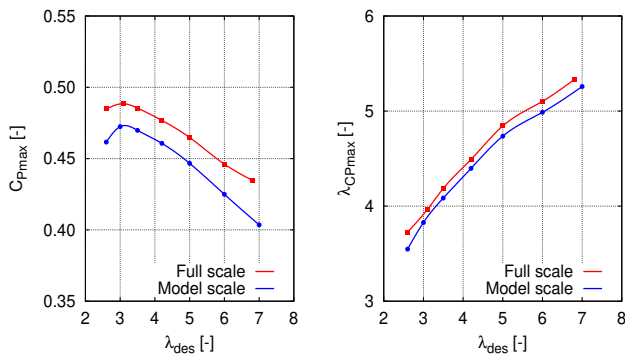


Fig. 24. Full-scale and model-scale turbine compared:  $C_{Pmax}$  (left) and  $\lambda_{CPmax}$  (right) as function of  $\lambda_{des}$ .

TABLE V  
FULL-SCALE AND MODEL-SCALE TURBINE COMPARED: MAIN GEOMETRY AND PERFORMANCE FIGURES.

	model scale	full scale
diameter	0.7 m	5.0 m
solidity	0.203	0.208
$C_{Pmax}$	0.473	0.488
$\lambda_{CPmax}$	3.89	3.95
$(C_P/C_T)_{max}$	0.529	0.534

As example of full-scale design results, the rotor corresponding to  $\lambda_{des} = 3.5$  is depicted in Fig. 26. Assuming a Maximum Power Point Tracking (MPPT) control strategy, Fig. 25 shows the calculated power-RPM curves at flow speed between 1.0 m/s (cut-in

speed) and rated-power condition at  $V_{des} = 2.5$  m/s. The maximum mechanical power output is 76.7 kW.

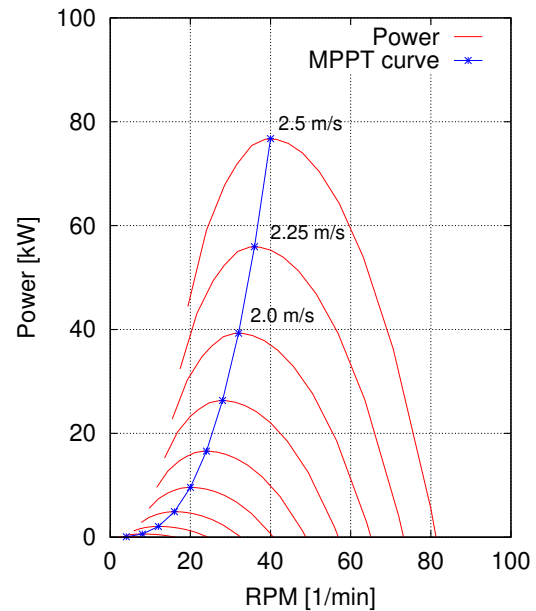


Fig. 25. Full-scale turbine,  $\lambda_{des} = 3.5$ : power-RPM curves as function of flow speed using a MPPT control ( $V_{des} = 2.5$  m/s).

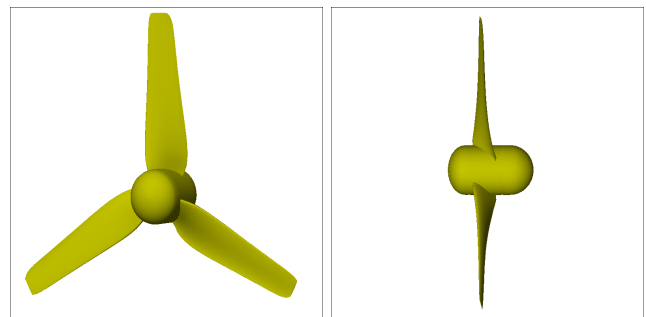


Fig. 26. Full-scale turbine geometry,  $\lambda_{des} = 3.5$ : front and side views (counter-clockwise rotating turbine).

Next, the effect on performance and operating conditions of results obtained at different  $\lambda_{des}$  is analyzed in Figs. 27 to 28. Specifically, three alternative design solutions corresponding to  $\lambda_{des} = 3.5, 5.0, 6.8$  are compared. Turbine mechanical power and torque over a

current speed range from cut-in speed  $V_{in} = 1.0$  m/s to cut-off speed  $V_{off} = 4$  m/s are given. Under overspeed conditions  $V > V_{des}$  it is assumed that the turbine is operated at rated power. Recalling performance results in Fig. 23, the maximum power coefficient is slightly decreasing with  $\lambda_{des}$ . This is confirmed in left Fig. 27. A more significant difference is observed in the peak torque that, under the considered control conditions, is achieved as the flow speed equals the design speed. Comparing power and torque curves in cases  $\lambda_{des} = 3.5$  and 6.8, it is found that a 10% reduction of rated power corresponds to more than 30% reduction of the peak torque. From the mechanical design viewpoint, a limitation of turbine torque obtained with the  $\lambda_{des} = 6.8$  design can be considered as a positive effect as the loading transferred to the powertrain is reduced.

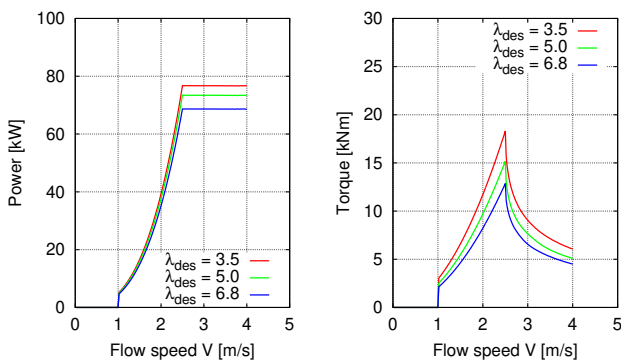


Fig. 27. Full-scale turbine,  $V_{des} = 2.5$  m/s: power (left) and torque (right) curves as function of flow speed.

For the same operating conditions, Fig. 28 presents turbine  $\lambda$  and rotational speed in RPM for the three  $\lambda_{des}$  cases. The trend to have higher peak power  $\lambda$  as  $\lambda_{des}$  increases is confirmed in left Fig. 28. This corresponds to a small difference in turbine RPM for operation at a flow speed up to  $V_{des}$ , whereas in overspeed conditions the turbine design corresponding to  $\lambda_{des} = 6.8$  operates at a powertrain speed significantly higher than the turbine with lower  $\lambda_{CPmax}$  ( $\lambda_{des} = 3.5$ ). The RPM difference is approximately 20%. From a hydrodynamic viewpoint, the design with the lower  $\lambda_{CPmax}$  should be preferred as it determines a slower rotational speed. At given inflow speed this results into a reduced risk of cavitation on rotor blades.

From the above discussion it follows that mechanical strength, powertrain sizing or hydrodynamic performance considerations may lead to opposed evaluations of alternative designs. The result of this simple analysis highlights that the selection of the *best* design stems from a complex decision making process where multidisciplinary aspects have to be taken into consideration.

For the sake of completeness, the energy assessment of the alternative turbine designs obtained by varying  $\lambda_{des}$  from 2.6 to 6.8 is presented in Fig. 29. The difference between the highest and lowest production results is approximately 10%. Results are referred to operation in calm water with an estimated capacity factor of 0.40. The site depth is 45 m and the 5 m diameter floating turbine is installed at depth of 7.5 m (Table IV). A

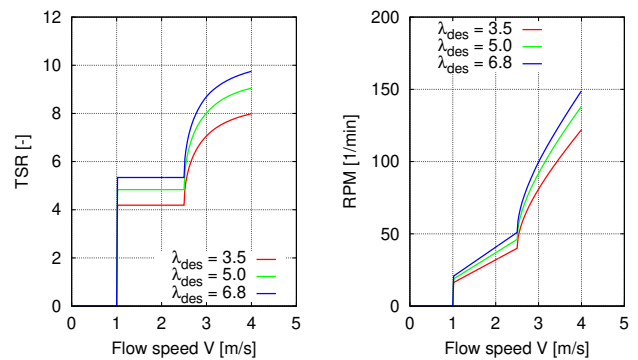


Fig. 28. Full-scale turbine,  $V_{des} = 2.5$  m/s: Tip Speed Ratio (TSR, left) and rotational speed (RPM, right) curves as function of flow speed.

standard  $z^n$  vertical velocity profile with  $n = 1/7$  has been considered.

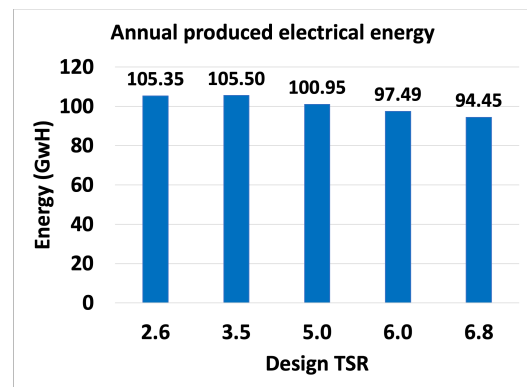


Fig. 29. Full scale turbine: annual electrical energy production. Design solutions for  $\lambda_{des}$  from 2.6 to 6.8 compared.

## VI. CONCLUSIONS

A computational procedure for the hydrodynamic design of horizontal-axis tidal turbines has been presented. The methodology combines an original design algorithm and a full 3D turbine hydrodynamics model.

Blade geometry parameters are determined with the objective to maximize power at given design Tip Speed ratio (TSR), whereas a constraint is introduced in order to limit turbine thrust at TSR higher than the design condition. With initial definitions of blade pitch and chord from 2D-flow hydrodynamics and momentum theory, radial distributions are iteratively modified to obtain the blade loading that satisfies requested conditions for power and thrust. At each iteration of the procedure, the guess turbine hydrodynamics is evaluated by a Boundary Integral Equation Method valid for arbitrary flows around 3D bodies. Differently to standard design methods based on blade element models, no 3D-flow corrections are necessary.

The capability of the proposed methodology to determine blade shapes matching imposed objectives and constraints is investigated by a numerical application to design a laboratory-scale 3-bladed turbine. A family of geometries is determined by varying the design TSR from 2.6 to 7. The highest peak power coefficient of 0.47 is determined at  $TSR = 3.9$ . This condition is found by

imposing a design TSR between 3 and 3.5. The identity between peak power TSR and design TSR is found at  $TSR = 4.6$ , where the peak power coefficient is 0.45. In all cases, the thrust coefficient constraint is satisfied.

Operational performance results have been further analysed by considering a second application addressing a 5 m diameter turbine in a real-world setting. As expected, a higher peak power coefficient compared to the model-scale turbine is obtained, as an effect of the higher Reynolds number. The analysis has been performed assuming a Maximum Power Point Tracking control strategy and constant-power operation at overspeed. Results of delivered torque, thrust, and corresponding RPM of alternative geometries obtained by varying the design TSR provide data to inform a dynamic decision-making process that takes into account several disciplines. As example, it is found that a 10% reduction of the annual energy production can be compensated by more than a 30% reduction of mechanical torque transferred to the powertrain in the peak power condition. Similarly, a relatively high design TSR allows to reduce axial loads while the power/thrust ratio is increased.

In the study, a high-camber profile has been taken as the baseline for the design of blade sections. More profiles with different characteristics are to be considered to assess the generality of the obtained results. Future applications of the design methodology will analyze the effect of rotor solidity by varying both blade chord distribution and the number of blades. Further developments of the methodology will also address the introduction of alternative constraints to control turbine operation factors as the negative pressure peak at blade leading edge in order to mitigate the risk of cavitation.

## REFERENCES

- [1] T. Burton, D. Sharpe, N. Jenkins, E. Bossanyi, "Wind energy handbook," Wiley and Sons, Chichester, England, 2001.
- [2] B. A. Mulugeta and A. Gerawork, "Aerodynamic design of horizontal axis wind turbine blades," *FME Transactions*, vol. 45, no. 4, pp. 647–660, 2017.
- [3] Y. M. El-Okda, "Design methods of horizontal axis wind turbine rotor blades," *International Journal of Industrial Electronics and Drives*, vol. 2, no. 3, pp. 135–150, 2015.
- [4] M. M. Duquette, J. Swanson, and K. D. Visser, "Solidity and blade number effects on a fixed pitch, 50 w horizontal axis wind turbine," *Wind Engineering*, vol. 27, no. 4, pp. 299–316, 2003.
- [5] N. Kaufmann, T. Carolus, and R. Starzmann, "Turbines for modular tidal current energy converters," *Renewable Energy*, vol. 142, pp. 451–460, 2019.
- [6] N. Kaufmann, T. Carolus, and R. Starzmann, "An enhanced and validated performance and cavitation prediction model for horizontal axis tidal turbines," *International journal of marine energy*, vol. 19, pp. 145–163, 2017.
- [7] J. Baltazar and J. Falcao de Campos, "Unsteady analysis of a horizontal axis marine current turbine in yawed inflow conditions with a panel method," in *1st International symposium on marine propulsors*, 2009.
- [8] F. Salvatore, Z. Sarichloo, and D. Calcagni, "Marine turbine hydrodynamics by a boundary element method with viscous flow correction," *Journal of Marine Science and Engineering*, vol. 6, no. 2, p. 53, 2018.
- [9] J. Baltazar, J. Machado, and J. Falcão de Campos, "Hydrodynamic analysis and analysis of horizontal axis marine current turbines with lifting line and panel methods," in *International Conference on Offshore Mechanics and Arctic Engineering*, vol. 44373, 2011, pp. 453–465.
- [10] J. B. Francisco Espenica, R.B. Santos Pereira and J. A. Falcão de Campos, "Design of a horizontal axis marine current turbine with dedicated hydrofoil sections," in *The Thirteenth European wave and Tidal Energy Conference*, 2019.
- [11] G. Dubbioso, F. Salvatore, Z. Sarichloo, D. Calcagni, R. Muscari, and R. Starzmann, "Variable-fidelity cfd modelling of horizontal-axis tidal turbines and arrays," in *The Thirteenth European wave and Tidal Energy Conference (EWTEC 19)*, 2019.
- [12] M. Drela, "Xfoil: An analysis and design system for low reynolds number airfoils," in *Low Reynolds number aerodynamics*. Springer, 1989, pp. 1–12.
- [13] Z. Sarichloo, F. Salvatore, F. Di Felice, M. Costanzo, R. Starzmann, and C. Frost, "Computational analysis and experimental verification of a boundary integral equation model for tidal turbines," in *Advances in Renewable Energies Offshore: Proceedings of the 3rd International Conference on Renewable Energies Offshore (RENEW 2018), October 8-10, 2018, Lisbon, Portugal*. CRC Press, 2018, p. 209.
- [14] F. Salvatore, Z. Sarichloo, and D. Calcagni, "A generalised boundary element method to analyse marine current turbines hydrodynamics including flow separation and stall," in *Fifth International Symposium on Marine Propulsors (SMP2017)*, Espoo, Finland, 2017.
- [15] A. Bahaj, A. Molland, J. Chaplin, and W. Batten, "Power and thrust measurements of marine current turbines under various hydrodynamic flow conditions in a cavitation tunnel and a towing tank," *Renewable energy*, vol. 32, no. 3, pp. 407–426, 2007.
- [16] M. Selig. (2021) Uiuic airfoil coordinates database. [Online]. Available: [https://m-selig.ae.illinois.edu/ads/coord\\_database.html](https://m-selig.ae.illinois.edu/ads/coord_database.html)
- [17] Institute of Marine Engineering, National Research Council of Italy (CNR-INM): Research facilities and laboratories. [Online]. Available: <http://www.inm.cnr.it/labs/>
- [18] T. M. El-Geziry, I. G. Bryden, and S. J. Couch, "Environmental impact assessment for tidal energy schemes: an exemplar case study of the strait of messina," *Journal of Marine Engineering and Technology*, vol. A13, pp. 39–48, 2009.
- [19] D. P. Coiro, G. Troise, and N. Bizzarrini, "Experiences in developing tidal current and wave energy devices for mediterranean sea," *Frontiers in Energy Research*, vol. 6, p. 136, 2018.
- [20] D. P. Coiro, G. Troise, N. Bizzarrini, G. Lazzarini, L. P. Di Noia, D. Iannuzzi, and C. Marino, "Design of gemstar tidal current fixed pitch rotor controlled through a permanent magnet generator (pmg) de-fluxing technique," *IET Renewable Power Generation*, vol. 14, no. 15, pp. 2897–2907, 2020.
- [21] G. Calcagno, F. Salvatore, L. Greco, A. Moroso, and H. Eriksson, "Experimental and numerical investigation of an innovative technology for marine current exploitation: the kobold turbine," in *Sixteenth International Offshore and Polar Engineering Conference, San Francisco, California, USA, May 2006*. ISOPE, 2006.
- [22] A. VV., *Tavole di Marea 2020*. Istituto Idrografico della Marina, Genoa, Italy, 2019 (in Italian).